ADVANCED ENERGY MATERIALS
www.advenergymat.de

Establishing Co-Continuous Network of Conjugated Polymers and Elastomers for High-Performance Polymer Solar Cells with Extreme Stretchability

*Jin-Woo Lee, Trieu Hoang-Quan Nguyen, Eun Sung Oh, Seungbok Lee, Jaeyoung Choi, Hyun Soo Kwon, Cheng Wang, Seungjin Lee, Jung-Yong Lee, Taek-Soo Kim, and Bumjoon J. Kim**

High power conversion efficiency (PCE) and mechanical robustness are prerequisites for wearable applications of organic solar cells (OSCs). However, stretchability of present active systems (i.e., crack-onset strain (COS) < 30%) should be improved. While introducing elastomers into active systems is considered a simple method for improving stretchability, the inclusion of elastomers typically results in a decrease in PCE of the OSC with a limited enhancement in the stretchability due to lack of interconnected electrical and mechanical pathways. In this study, it is developed efficient and intrinsically stretchable (IS)-OSCs with exceptional mechanical robustness, by constructing co-continuous networks of conjugated polymers (D18) and elastomers (SEBS) within active layers. It is demonstrated that the blend film with a specific ratio (40:60 w/w) of D18:SEBS is crucial for forming co-continuous structures, establishing well-connected mechanical and electrical channels. Consequently, $D18_{0.4}$:$SEBS_{0.6}$/L8-BO OSCs achieve 16-times higher stretchability (COS = 126%) than the OSCs based on D18/L8-BO (COS = 8%), while achieving 4-times higher PCE (12.13%) compared to the OSCs based on SEBS-rich active layers ($D18_{0.2}$:$SEBS_{0.8}$/L8-BO, PCE = 3.15%). Furthermore, $D18_{0.4}$:$SEBS_{0.6}$-based IS-OSCs preserve 86 and 90% of original PCEs at 50% strain and after 200 stretching/releasing cycles with 15% strain, respectively, demonstrating the highest mechanical robustness among reported IS-OSCs.

1. Introduction

Organic solar cells (OSCs) are promising renewable energy sources owing to their lightweight, mechanical flexibility, semi-transparency, and ease of processing.[1] In recent years, the power conversion efficiencies (PCEs) of OSCs have exceeded 19%, thanks to the development of various polymer donors (P_Ds) and small molecule acceptors (SMAs).[2] However, the intrinsic brittleness of rigid P_Ds and SMAs hampers the wearable applications of the resulting OSCs necessitating resilience to repetitive body motions, which require high stretchability of at least 50% in any direction for stable operation.[3] The key reason causing this brittleness lies in the formation of unconnected, excessively large crystalline domains within the active layers, as a consequence of the stiffness inherent in the backbones of P_Ds and SMAs.[4] Although different molecular design strategies, including the synthesis of conjugated polymers with very high molecular weights and less rigid backbones or the

J.-W. Lee, T. H.-Q. Nguyen, J. Choi, H. S. Kwon, B. J. Kim
Department of Chemical and Biomolecular Engineering
Korea Advanced Institute of Science and Technology (KAIST)
Daejeon 34141, Republic of Korea
E-mail: bumjoonkim@kaist.ac.kr

The ORCID identification number(s) for the author(s) of this article can be found under https://doi.org/10.1002/aenm.202401191

DOI: 10.1002/aenm.202401191

E. S. Oh, T.-S. Kim
Department of Mechanical Engineering
Korea Advanced Institute of Science and Technology (KAIST)
Daejeon 34141, Republic of Korea

S. Lee, J.-Y. Lee
School of Electrical Engineering
Korea Advanced Institute of Science and Technology (KAIST)
Daejeon 34141, Republic of Korea

C. Wang
Advanced Light Source
Lawrence Berkeley National Laboratory
1 Cyclotron Road, Berkeley, CA 94720, USA

S. Lee
Advanced Energy Materials Research Center
Korea Research Institute of Chemical Technology (KRICT)
Daejeon 34114, Republic of Korea

design of P_D/SMA with improved miscibility, have been recently suggested to improve the stretchability of the active layer, the stretchability (i.e., crack-onset strain (COS)) of the high-performance active layers typically remains below 30%.[5]

Incorporating elastomers such as poly(dimethylsiloxane) (PDMS) or polystyrene-*block*-poly(ethylene-*ran*-butylene)-*block*-polystyrene (SEBS) as a third component in the photoactive layers is an effective strategy to enhance their stretchability.[5a,6] Elastomers with soft backbone structures often show very high stretchability (ϵ) of over 500% due to their low glass-transition temperature (T_g) and low critical molecular weight (M_c) of below 10-20 kg mol^{-1}, facilitating the formation of entangled chains in the films.[7] Thus, researchers have demonstrated examples of enhancing the stretchability of OSCs by the addition of the elastomers.[5a,6a–c,e,f] For example, Ye group first reported the design strategy of adding the SEBS polymers as a ternary constituent into the PM6:N3 system.[5a] They reported a 2-fold increase in the COS values from 6.9 to 13.0% by 30 wt% SEBS addition, while the PCE value decreased from 15.42% to 11.55%. In a subsequent study, they introduced a higher concentration of SEBS (> 40 wt%) into the PM6:PYFT-o system.[6b] This addition significantly increased the stretchability of the active layer, but also resulted in the PCE decrease. While the pristine PM6:PYFT-o-based OSC had a PCE of 14.9% and a COS of 4.7%, the ternary OSCs with 33.3 wt% of SEBS showed a PCE of 11.3% and COS of 26.2%. Furthermore, the ternary OSCs with 90.9 wt% of SEBS exhibited a remarkable COS of 1031%, but a low PCE of 2.2%. At an optimal SEBS composition of 41 wt%, the COS value of the ternary active layer was increased to 51%, and the resulting OSC maintained a relatively high PCE of ≈10%. Subsequently, O'Connor group incorporated SEBS polymers as a third component in the PM6:Y6 host binary blend.[6c] They observed that adding 20 wt% SEBS polymers to the active layers increased the fracture energy from 2 to 12 J m^{-2}, albeit with a reduction in PCE from 12.72% to 9.10%. Given the insights from these examples, it is anticipated that the strategy of incorporating elastomers can be extended to a wide range of active systems.[5j,6c,8] While significant progress in enhancing the mechanical robustness of high-performance active layers has been made by various approaches,[5a,6a–c,f,8b,9] it still remains a grand challenge to avoid the compromise between the photovoltaic performance and mechanical robustness in OSCs. The significant decrease in the PCE value by addition of elastomers is primarily due to two reasons: 1) dilution of the photoactive materials by addition of non-photoactive materials deteriorates the light harvesting capability of the OSCs; 2) disconnection of charge transporting pathways by increased amount of the elastomer phase hinders the hole/electron transport and increases the undesired charge recombination in the active layer.

To achieve both high electrical and mechanical properties, interconnected networks of both elastomers and conjugated polymers, which can act as mechanical scaffold and charge transporting pathway, respectively, should be achieved within the active layer. The percolation threshold in polymer blends is a critical composition ratio at which one polymer, present in a lesser amount than the other, percolates to form connected networks throughout the other primary polymer matrix.[10] At this threshold, the minor polymer component starts to form a connected structure, generating pathways for electrical or mechanical function and significantly enhancing the electrical conductivity or mechanical strength of the polymer blend.[10a,c] This phenomenon has been observed in various conducting polymers within insulating polymer composites.[10c–e,11] For example, increasing the weight fraction of conjugated polymers into an insulating polymer matrix beyond the percolation threshold can result in a rapid increase in conductivity and charge mobility by over 3–4 orders of magnitude.[10a,d,12] Conversely, when conjugated polymers constitute a substantial part of the blends, mechanical stretchability is significantly enhanced at the percolation threshold of elastomers due to the formation of a network structure across the conjugated polymer domains.[12b,c,13] This structure establishes a mechanical scaffold for efficient stress dissipation. When the composition ratios in the conjugated polymer/elastomer blends are positioned over both the electrical and mechanical percolation thresholds, the polymer blend can exhibit a co-continuous structure. In this morphology, two polymers are continuously percolated to one another, comprising crystalline fibrils of conjugated polymers for charge transport and continuous elastomer networks for mechanical stress dissipation. Therefore, we anticipate that finding the thresholds for forming co-continuous structure of elastomers within the photoactive layer is crucial for optimizing the mechanical stretchability and PCEs of the OSCs.

In this study, we demonstrate efficient OSCs with extreme stretchability (COS = 126%) and high PCE (>12%) by developing photoactive layers with co-continuous structure of conjugated polymers (D18) and thermoplastic elastomers (SEBS). To achieve superior photovoltaic and mechanical properties, we construct photoactive layers featuring a planar-heterojunction (PHJ) architecture comprising vertically interdiffused D18:SEBS bottom layers and L8-BO top layers, and fine-tune the composition ratios of D18 and SEBS within the bottom layers ($D18_x$:$SEBS_{1.0-x}$, x ranging from 0 to 1.0). We demonstrate that at a specific composition ratio of D18:SEBS = 40:60 w/w, co-continuous blend morphologies are produced, achieving both high photovoltaic and mechanical properties of the OSCs. The active layers with this optimal composition ratio ($D18_{0.4}$:$SEBS_{0.6}$/L8-BO) achieve a 16-times higher stretchability (COS = 126%) compared to the reference D18/L8-BO (COS = 8%), and a 4-times higher PCE (12.13%) relative to active layers rich in SEBS ($D18_{0.2}$:$SEBS_{0.8}$/L8-BO, PCE = 3.15%). Based on comprehensive morphological investigations, we demonstrate that the co-achievements of high PCE and stretchability of $D18_{0.4}$:$SEBS_{0.6}$/L8-BO are attributed to the establishment of well-connected electrical and mechanical channels facilitated by the co-continuous networks of D18 and SEBS within the PHJ-type active layers. To demonstrate potential applications in wearable devices, we fabricate IS-OSCs using the $D18_{0.4}$:$SEBS_{0.6}$/L8-BO-based active layers. The $D18_{0.4}$:$SEBS_{0.6}$/L8-BO-based IS-OSCs exhibit a remarkable device stretchability (86% retention of initial PCE at 50% strain) and cyclic durability (90% retention of initial PCE after 200-times stretching/releasing cycles with 15% strain).

2. Results and Discussion

2.1. Research System and Basic Material Properties

Conventional OSCs based on high-performance P_D:SMA blends are typically brittle (COS < 5%), limiting their application into

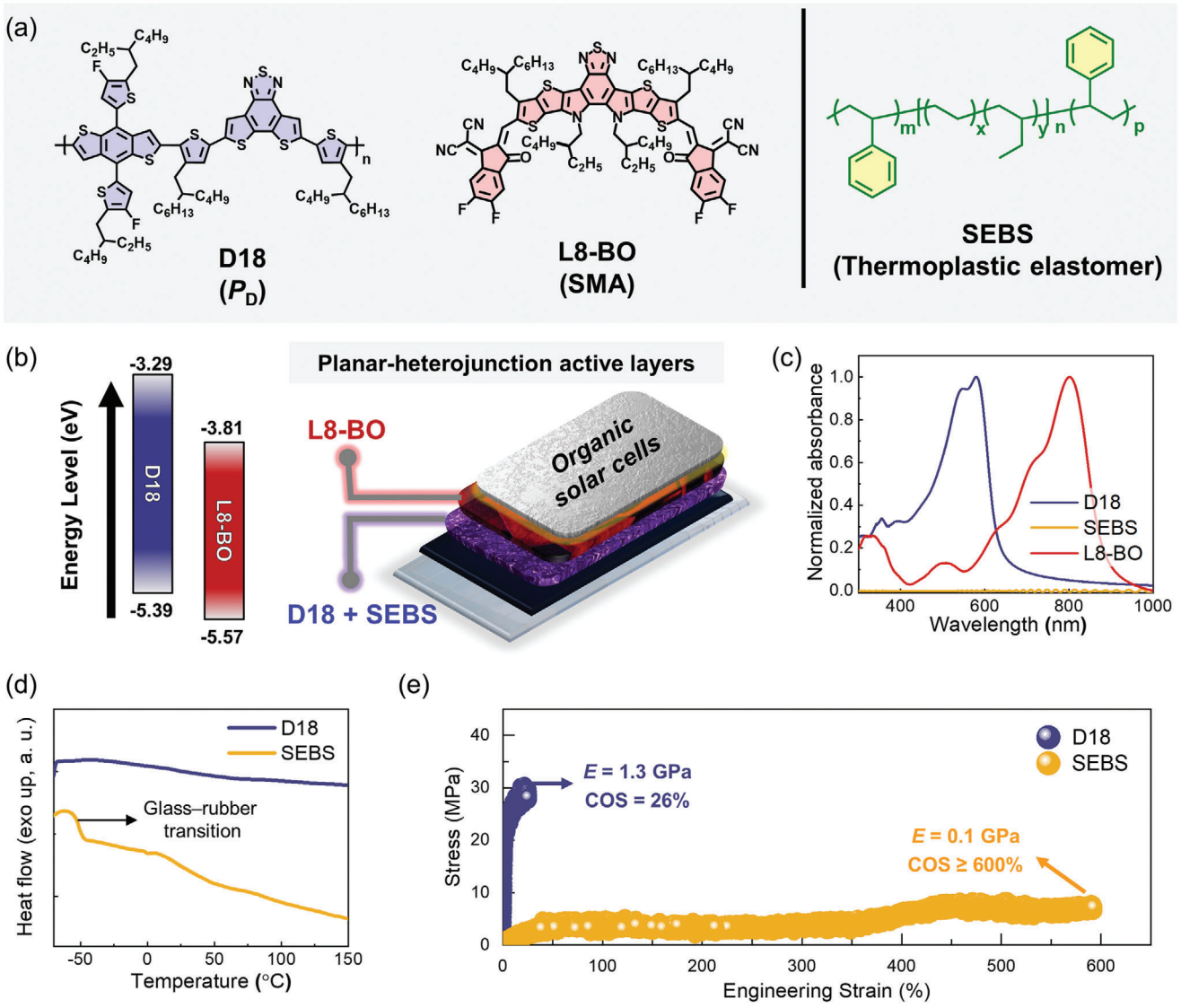

Figure 1. a) Chemical structures of P_D (D18), SMA (L8-BO), and thermoplastic elastomer (SEBS). b) Energy levels of the active components and device structure of the rigid OSCs. c) UV–vis absorption spectra in film of the materials used in this study, d) DSC curves (2nd heating cycle), and e) stress–strain curves of pristine films obtained from pseudo free-standing tensile tests.

wearable devices. The mechanical brittleness is mainly due to large, disconnected crystalline domains of the P_D and SMA owing to their rigid backbone structures, which are designed to achieve high electrical and photovoltaic properties. Incorporation of highly stretchable elastomers (i.e., PDMS, SEBS, and polyurethane) into P_D:SMA blends is a simple method for improving the stretchability of the active layers. However, this strategy often sacrifices the PCE of the OSCs while not significantly increasing their stretchability, which is due to lack of well-connected electrical and mechanical channels. Therefore, we believe that the formation of co-continuous networks between conjugated polymers and elastomers, where the two polymer domains interpenetrate to each other, will be critical for achieving both high PCE and mechanical robustness of the OSCs. In addition, we employ a strategy of pseudo planar-heterojunction (PHJ) structure consisting of P_D:elastomer bottom layer and SMA top layer, but the layers are interdiffused to facilitate vertical hole/electron transport from the active layer to the electrode while ensuring the high adhesion between the layers.[5f,14]

To systematically examine the phase behaviors between conjugated polymers and elastomers as well as correlate them with photovoltaic and mechanical properties of the OSCs, we design a model system using well-known P_D, SMA, and thermoplastic elastomer. Chemical structures of the materials used in this study are presented in **Figure 1**a. We selected D18 and L8-BO as high-performance P_D and SMA materials, respectively, as these active components were reported to demonstrate OSCs with high PCEs of ≈18% in literatures.[2a,d] We also selected SEBS as the elastomer component owing to its excellent stretchability, low cost, and common use for various commercial applications.[15] Furthermore, distinct from other elastomers such as PDMS, SEBS has the unique ability to produce fibril

structures, which can promote its percolation within the matrix of conjugated polymers.[10c,16] Chemical structure of the SEBS used in this study, composed of 5.8, 56.5, and 37.7 mol.% of styrene, ethylene, and butylene components, respectively, was confirmed by ^{1}H nuclear magnetic resonance (NMR) spectra (Figure S1, Supporting Information). Molecular weight information of D18 and SEBS polymer was obtained from size-exclusion chromatography (SEC) measurements (Figure S2, Supporting Information). The D18 and SEBS had number-average molecular weight (M_n)/dispersity ($Đ$) values of 85 kg mol^{-1}/2.7 and 164 kg mol^{-1}/1.1, respectively. Optical and electrochemical properties of the materials were characterized by measuring cyclic voltammetry (CV) and ultraviolet-visible (UV–vis) light absorption spectra (Figure 1b,c; Figure S3, Supporting Information). D18 and L8-BO exhibited well-matched highest occupied molecular orbital (HOMO) and lowest unoccupied molecular orbital (LUMO) energy levels for efficient exciton dissociation (Figure 1b). In addition, D18 and L8-BO showed complementary light absorption profiles, enabling their efficient charge generation (Figure 1c). The SEBS did not exhibit bandgap or UV–vis absorbances due to the absence of conjugation in the backbone structures.

In this study, we employed PHJ-structured active layers (D18$_x$:SEBS$_{1.0-x}$/L8-BO) where the SMA (L8-BO) top layer is deposited on the bottom layer of P_D:elastomer (D18$_x$:SEBS$_{1.0-x}$), because the PHJ-structured active layer can be more efficient in terms of mechanical stress dissipation and vertical charge transport compared to the bulk-heterojunction (BHJ) structure.[5f,14] In addition, by implementing the PHJ structure, we can gain insight into how the D18:SEBS morphology impacts the photovoltaic and mechanical properties of OSCs. To ensure sufficient adhesion/interfacial properties between the lower and upper layers within the PHJ active layers, we employed different solvents for the processing of each layer and generated sufficient intermixed zone between the layers. Specifically, the D18$_x$:SEBS$_{1.0-x}$ bottom layer was spin-coated using chloroform. Subsequently, the L8-BO top layer was deposited using carbon tetrachloride as the solvent, which partially but not fully dissolves the D18$_x$:SEBS$_{1.0-x}$ bottom layer. As a result, the D18$_x$:SEBS$_{1.0-x}$ and L8-BO layers were vertically interdiffused, forming the intermixed zone near their interfaces in the PHJ films, as evidenced by gradient concentrations within the vertical concentration profiles obtained by the time-of-flight secondary ion mass spectrometry (ToF-SIMS) (Figure S4, Supporting Information). Utilizing the half-depth point identified in the ToF-SIMS profiles as a reference, the thickness values of the L8-BO-rich and D18-rich layers within the PHJ-type active layers were estimated to be ≈50 and 70 nm, respectively. The vertically interdiffused structure not only broadens the interfaces between the bottom–top layers, but also significantly improves their adhesion, thereby maximizing capabilities of the PHJ films for mechanical stress dissipation and charge generation/transport. To systematically investigate the phase behaviors of D18 and SEBS in their blend films, the weight composition of D18 in the bottom layer was varied from 0 to 100% (D18$_x$:SEBS$_{1.0-x}$, where x = 0 to 1.0), while the fabrication conditions of L8-BO in the top layer remained constant. The molar fraction (N) of D18 in the blends at each corresponding weight composition was estimated using their M_n values (Table S2, Supporting Information).

Thermal properties of D18, L8-BO, and SEBS were monitored by differential scanning calorimetry (DSC) measurements (Figure 1d; Figure S5, Supporting Information). D18 polymer and L8-BO SMA did not show T_g signal due to their strong crystalline properties. In contrast, the SEBS polymers exhibited a clear T_g at −55 °C in a DSC 2nd heating profile. This sub-zero T_g originates from the poly(ethylene-*ran*-butylene) soft segments in the SEBS block-copolymers.[17] Mechanical properties of the materials in thin film were investigated by pseudo free-standing tensile tests on water surfaces (Figure 1e). Without the influence of thick substrates, this experimental setup can acquire intrinsic tensile characteristics of thin films.[18] Owing to their soft backbone structures and low T_g, the SEBS elastomers exhibited significantly higher stretchability and lower elastic modulus (E) compared to conventional conjugated polymers including D18. For example, SEBS film was not fractured until the strain limit of the experiment set-up (≈600%) and exhibited a low E of 0.1 GPa. In contrast, the D18 film was fractured at 23% strain and exhibited a higher E of 1.3 GPa. The tensile properties of L8-BO could not be measured by this tensile testing method due to their extreme brittleness.

2.2. Photovoltaic Properties

To investigate the effect of D18:SEBS contents on the photovoltaic performances of OSCs, we fabricated OSC devices with a normal-type device configuration (**Figure 2**a–c). The detail conditions for OSC fabrications are described in the Supporting Information. Current density–voltage (J–V) curves and corresponding photovoltaic parameters are shown in Figure 2a and **Table 1**, respectively. The reference D18/L8-BO-based PHJ OSCs exhibited a high PCE of 17.48%, with open-circuit voltage (V_{oc}), short-circuit current density (J_{sc}), and fill factor (FF) values of 0.88 V, 25.57 mA cm^{-2}, and 0.77, respectively. The PCE of the OSCs was almost unchanged until 20 wt% of SEBS content was added (i.e., D18$_{0.8}$:SEBS$_{0.2}$/L8-BO PHJ OSC), with a slight enhancement noted with the addition of 10 wt% SEBS. Specifically, the PCE for the D18$_{0.9}$:SEBS$_{0.1}$/L8-BO and D18$_{0.8}$:SEBS$_{0.2}$/L8-BO-based OSCs was 17.68% and 17.40%, respectively. The improvement and retention of PCE with a minimal SEBS incorporation can be attributed to the nanoconfinement effects on D18 domains, which lead to an increase in crystallinity and hole mobility. This phenomenon is discussed in further detail in the following section. Then, the PCE value showed a gradual decline with further increase of SEBS content to 60 wt% (i.e., D18$_{0.4}$:SEBS$_{0.6}$/L8-BO PHJ OSC). For example, the PCEs of the OSCs with 20 wt%, 40 wt%, and 60 wt% of the SEBS contents were 17.40%, 15.22%, and 12.13%, respectively. The main parameters contributing to the PCE trend were J_{sc} and FF. Interestingly, we found that PHJ-type devices had considerably greater PCE tolerances to SEBS inclusion than BHJ-type devices (Figure S6 and Table S3, Supporting Information). For example, PCE values of D18$_{0.4}$:SEBS$_{0.6}$-based PHJ and BHJ devices were 12.13 and 6.65%, respectively, while their initial PCEs without SEBS were similar (17.48%–17.72%). However, the PCE decreases of the PHJ-type OSCs became significantly accelerated when the SEBS content exceeded 60 wt% (Figure 2c). The PCEs of OSCs based on D18$_{0.3}$:SEBS$_{0.7}$/L8-BO, D18$_{0.2}$:SEBS$_{0.8}$/L8-BO,

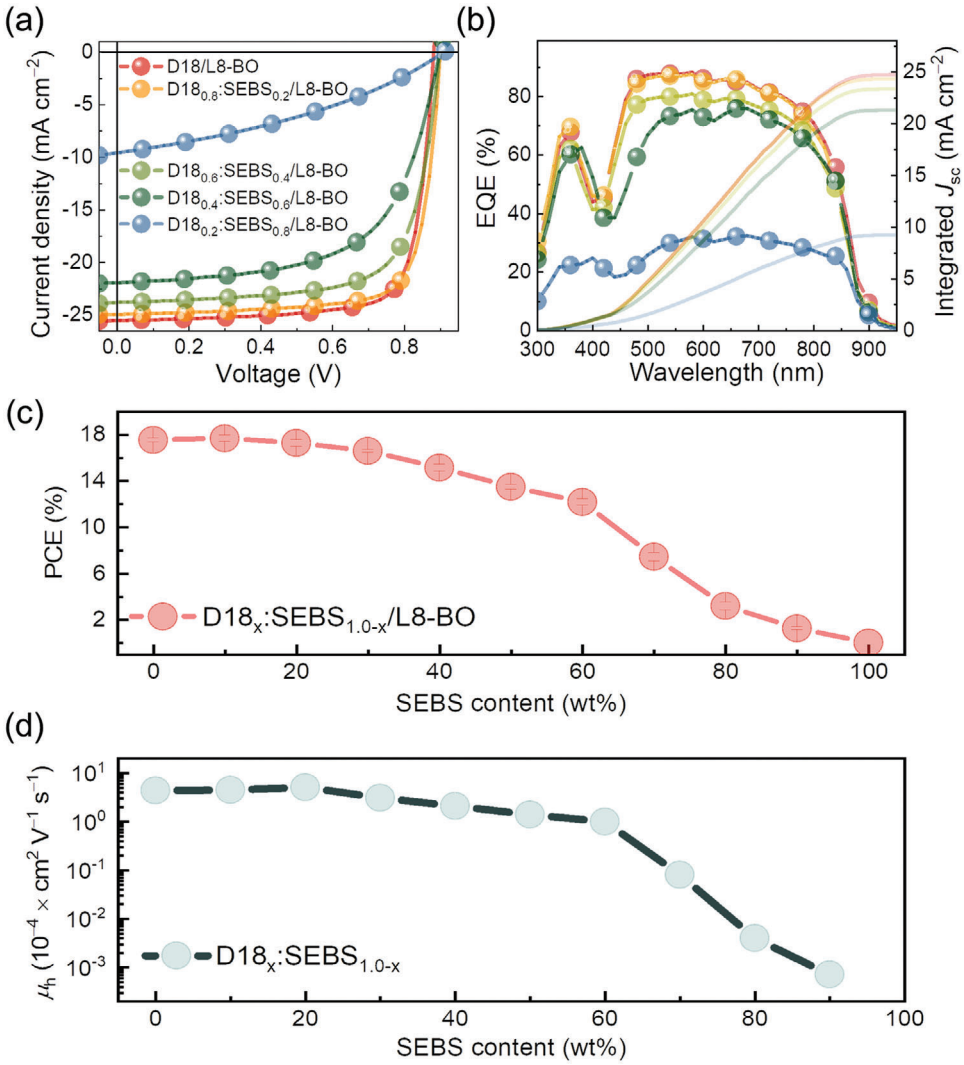

Figure 2. a) *J–V* curves, and b) EQE spectra, c) PCE values, and d) SCLC hole mobilities (μ_h) of D18:SEBS/L8-BO OSCs at varying D18:SEBS composition ratios.

Table 1. Photovoltaic performances of D18:SEBS/L8-BO OSCs.

P_D:elastomer	V_{oc} [V]	J_{sc} [mA cm^{-2}]	*Cal.* J_{sc} [mA cm^{-2}][a)]	FF	PCE$_{max(avg)}$[b)] [%]	PCE/$v_{D18+L8-BO}$[c)] [%]
D18	0.88	25.57	24.73	0.77	17.48 (17.12)	17.48
D18$_{0.9}$:SEBS$_{0.1}$	0.90	25.87	25.18	0.78	17.68 (17.31)	18.04
D18$_{0.8}$:SEBS$_{0.2}$	0.90	25.12	24.65	0.77	17.40 (17.08)	18.32
D18$_{0.7}$:SEBS$_{0.3}$	0.90	24.63	24.13	0.75	16.54 (16.23)	18.18
D18$_{0.6}$:SEBS$_{0.4}$	0.90	23.86	23.45	0.71	15.22 (14.90)	17.49
D18$_{0.5}$:SEBS$_{0.5}$	0.90	22.41	21.84	0.65	13.11 (12.88)	15.80
D18$_{0.4}$:SEBS$_{0.6}$	0.90	21.99	21.30	0.61	12.13 (11.94)	15.55
D18$_{0.3}$:SEBS$_{0.7}$	0.90	15.13	14.73	0.50	7.56 (7.29)	10.36
D18$_{0.2}$:SEBS$_{0.8}$	0.91	9.62	9.18	0.36	3.15 (2.88)	4.70
D18$_{0.1}$:SEBS$_{0.9}$	0.91	4.82	4.64	0.29	1.27 (1.04)	2.15
SEBS	0.37	0.48	–	0.25	0.04 (0.03)	0.08

[a)] Calculated from EQE spectra; [b)] Average values obtained from 15 independent devices; [c)] PCE$_{max}$ values divided by the respective volume fraction of (D18+L8-BO) active components in D18$_x$:SEBS$_{1.0-x}$/L8-BO PHJ active layers.

and $D18_{0.1}$:$SEBS_{0.9}$/L8-BO were 7.56%, 3.15%, and 1.27%, respectively. And the main parameters causing the PCE drops were J_{sc} and FF. External quantum efficiency (EQE) spectra of the OSCs are shown in Figure 2b. The calculated J_{sc} values of the OSCs from the EQE spectra agree well with the device J_{sc}s within a 4% error.

To emphasize the advantages of the $D18_x$:$SEBS_{1.0-x}$/L8-BO PHJ devices, we calculated the PCE/$\nu_{D18+L8-BO}$ metric, where the PCE values of the devices were normalized by the volume fraction ($\nu_{D18+L8-BO}$) of the (D18+L8-BO) active components within the active layer (Table 1; Table S2, Supporting Information). Although the calculated $\nu_{D18+L8-BO}$ may not exactly match the real volume fraction, the estimated parameter PCE/$\nu_{D18+L8-BO}$ provides an insightful measure of the practical PCE when considering the cost of active components and elastomers. It is noted that the elastomers are at least 100 times cheaper than any of the active components. The PCE/$\nu_{D18+L8-BO}$ values of $D18_x$:$SEBS_{1.0-x}$/L8-BO with 10 wt%–30 wt% of SEBS contents were higher than 18%, exceeding that of the D18/L8-BO system without SEBS (PCE/$\nu_{D18+L8-BO}$ = 17.48%). Furthermore, even up to 60 wt% SEBS content, the PCE/$\nu_{D18+L8-BO}$ remained above 15%, suggesting that the cost-PCE balance of $D18_{0.4}$:$SEBS_{0.6}$/L8-BO active layers is comparable to that of typical active layers with more than 15% PCE. This demonstrates the feasibility of the developed active layer system for commercial applications.

Charge transport properties of the $D18_x$:$SEBS_{1.0-x}$ blend films with different D18:SEBS ratios were probed by measuring space-charge limited current (SCLC) hole mobility (μ_h) (Figure 2d and Table S4, Supporting Information).[19] Pristine D18 exhibited a high μ_h value of 4.4 $\times 10^{-4}$ cm^2 V^{-1} s^{-1}. Interestingly, we observed that the μ_h of the blend films slightly increased with 20 wt% SEBS addition. For example, the μ_h value of $D18_{0.8}$:$SEBS_{0.2}$ film was 5.1 $\times 10^{-4}$ cm^2 V^{-1} s^{-1}. Then, the μ_h value decreased with increasing the SEBS content to 60 wt%. When the SEBS content exceeded 60 wt%, the μ_h rapidly dropped, which agrees well with the PCE trend in OSC devices. Specifically, the μ_h values of $D18_{0.6}$:$SEBS_{0.4}$, $D18_{0.4}$:$SEBS_{0.6}$, and $D18_{0.2}$:$SEBS_{0.8}$ films were 2.1 $\times 10^{-4}$, 1.0 $\times 10^{-4}$, and 4.3 $\times 10^{-7}$ cm^2 V^{-1} s^{-1}, respectively. The increase in μ_h of $D18_x$:$SEBS_{1.0-x}$ blend films with low (10 wt%–20 wt%) SEBS contents compared to the pure D18 film is likely due to improved molecular orderings and crystallinity of D18 domains due to nanoconfinement effects from the SEBS addition.[20] For example, in UV-Vis absorption spectra of $D18_x$:$SEBS_{1.0-x}$ blend films, both the maximum absorption wavelength (λ_{max}^{film}) and relative absorbance of (0-0) transition peak (≈590 nm) to that of (0-1) peak (≈550 nm) ($I_{(0-0)}/I_{(0-1)}$) linearly increased with higher SEBS fractions; D18 (λ_{max}^{film} = 579 nm and $I_{(0-0)}/I_{(0-1)} = 1.06$) < $D18_{0.8}$:$SEBS_{0.2}$ (λ_{max}^{film} = 583 nm and $I_{(0-0)}/I_{(0-1)} = 1.12$) < $D18_{0.6}$:$SEBS_{0.4}$ (λ_{max}^{film} = 585 nm and $I_{(0-0)}/I_{(0-1)} = 1.16$) < $D18_{0.4}$:$SEBS_{0.6}$ (λ_{max}^{film} = 586 nm and $I_{(0-0)}/I_{(0-1)} = 1.20$) (Figure S7, Supporting Information). This indicates increased degree of molecular orderings of D18 in $D18_x$:$SEBS_{1.0-x}$ blend films with higher SEBS contents. The relatively slow decrease in μ_h with increasing the SEBS content in the range of 20 wt%–60 wt% is due to the gradual decrease in the area density of the D18 network by added electrically-inactive SEBS elastomers in the blend films. In contrast, the sharp drop in μ_h beyond 60 wt% SEBS content, unlike the moderate decreases observed between 20 wt% to 60 wt% SEBS content, suggests a disruption in the charge transport network of the D18 domains in the blend films. The L8-BO film exhibited an electron mobility (μ_e) of 4.0 $\times 10^{-4}$ cm^2 V^{-1} s^{-1}. As a result, the μ_e/μ_h values of the blend films drastically increased when the SEBS content exceeds 60 wt%. In detail, the μ_e/μ_h values of D18, $D18_{0.8}$:$SEBS_{0.2}$, $D18_{0.6}$:$SEBS_{0.4}$, $D18_{0.4}$:$SEBS_{0.6}$, and $D18_{0.2}$:$SEBS_{0.8}$ were 0.9, 0.8, 1.9, 4.4, and 1023, respectively. The abysmal μ_h values and unbalanced μ_e/μ_h of the $D18_x$:$SEBS_{1.0-x}$ blend films exceeding 60 wt% SEBS contents correspond to their poor J_{sc}, FF, and PCE values in the OSC devices.[6c,21]

Table 2. Tensile properties of $D18_x$:$SEBS_{1.0-x}$/L8-BO PHJ films.

PHJ films	COS [%][a]	E [GPa] [a]	Toughness [MJ m^{-3}] [a]
D18/L8-BO	8	1.8	2.2
$D18_{0.8}$:$SEBS_{0.2}$/L8-BO	12	1.4	2.9
$D18_{0.6}$:$SEBS_{0.4}$/L8-BO	17	1.1	3.3
$D18_{0.4}$:$SEBS_{0.6}$/L8-BO	126	0.7	17.5
$D18_{0.2}$:$SEBS_{0.8}$/L8-BO	> 600	0.2	> 25
SEBS/L8-BO	> 600	0.1	> 25

[a] Averaged values from 3 independent samples.

2.3. Mechanical Properties

Next, we investigated the mechanical properties of $D18_x$:$SEBS_{1.0-x}$/L8-BO PHJ films with various D18:SEBS composition ratios using pseudo free-standing tensile tests (Figure 3a–c and **Table 2**). The measured COS values, PCE versus COS plots, and stress–strain (S–S) curves of the PHJ thin-films as a function of D18:SEBS content are displayed in **Figure 3a–c**, respectively. The detailed tensile parameters including COS, elastic modulus (E), and toughness are summarized in Table 2.

The $D18_x$:$SEBS_{1.0-x}$:L8-BO PHJ films exhibited gradual increase of COS and decrease of E as the SEBS concentration increased from 0 to 40 wt%. For example, the COS values of the blend films increased from 8 to 17%, whereas E reduced from 1.8 to 1.1 GPa from 0 wt% to 40 wt% of the SEBS contents. As a result, the $D18_x$:$SEBS_{1.0-x}$:L8-BO PHJ films with 0 wt%–40 wt% of SEBS exhibited similar toughness values (2.2–3.3 MJ m^{-3}). Furthermore, the increase in stretchability of $D18_x$:$SEBS_{1.0-x}$/L8-BO films with the SEBS contents of 10 wt%–40 wt% relative to the D18/L8-BO film was less than 10% in the COS value, which is not significant considering exceptionally high stretchability of SEBS elastomers with COS of > 600%. However, it was observed that the stretchability and toughness of $D18_x$:$SEBS_{1.0-x}$:L8-BO PHJ films dramatically increased when the SEBS content became 60 wt%. For example, the $D18_{0.4}$:$SEBS_{0.6}$/L8-BO PHJ film had a COS value of 126% and toughness value of 17.5 MJ m^{-3}. Furthermore, the PHJ films containing SEBS content higher than 70 wt% (i.e., $D18_{0.8}$:$SEBS_{0.2}$/L8-BO and SEBS/L8-BO films) were not fractured at the measurement limit of 600% strain. And they exhibited toughness values exceeding 25 MJ m^{-3}. Therefore, in terms of both the photovoltaic and mechanical properties, we highlight that the $D18_{0.4}$:$SEBS_{0.6}$ blend film achieved both a high PCE (12.13%) and excellent stretchability (COS = 126%) (Figure 3b). The stretchability of $D18_{0.4}$:$SEBS_{0.6}$/L8-BO was 16 times higher compared to that of D18/L8-BO films (COS

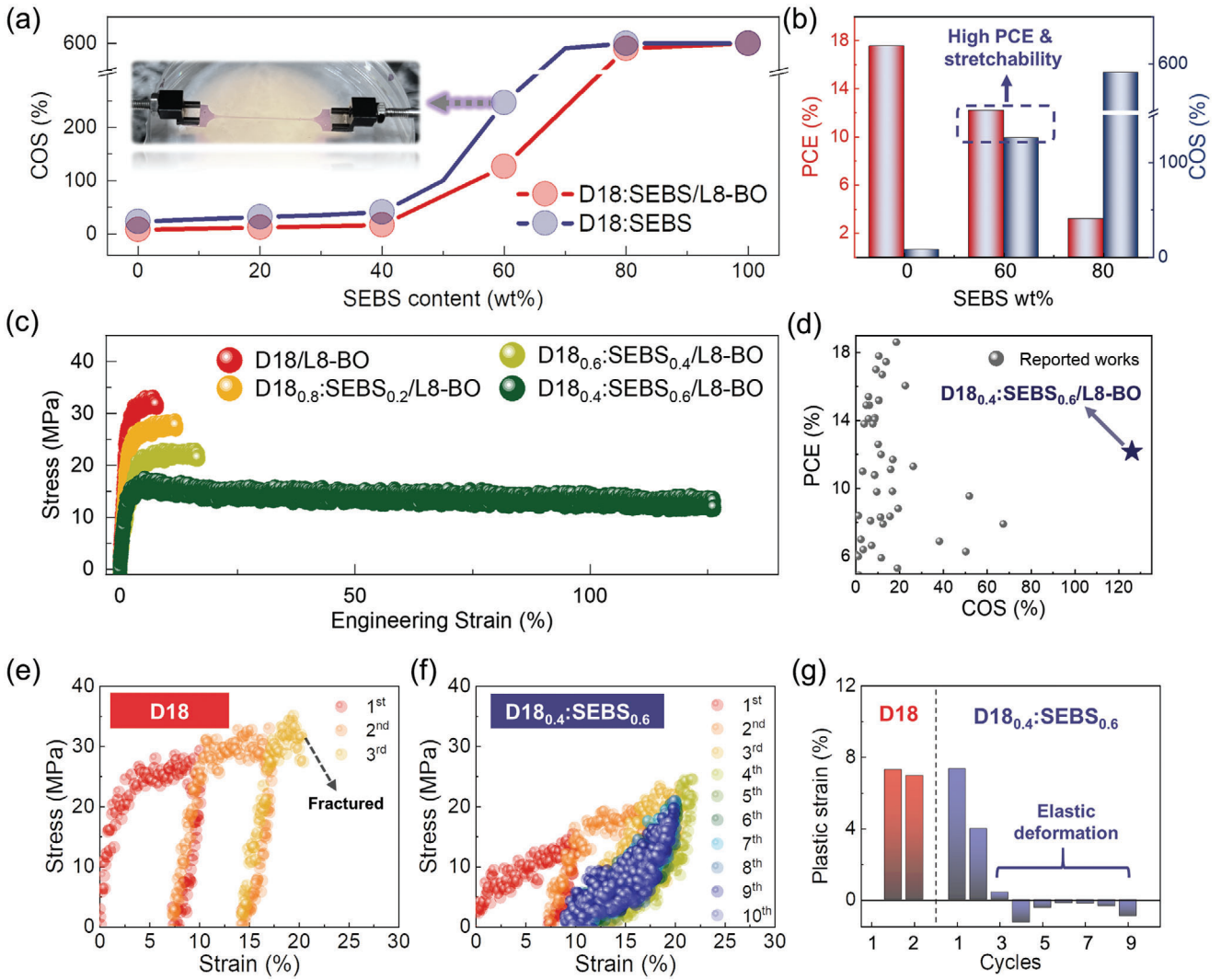

Figure 3. a) COS values of D18$_x$:SEBS$_{1.0-x}$ blend films (blue lines) and D18$_x$:SEBS$_{1.0-x}$/L8-BO PHJ films (red lines). b) PCE versus COS plots and c) stress–strain (*S–S*) curves of D18$_x$:SEBS$_{1.0-x}$/L8-BO PHJ films. d) PCE and COS in this work and other works (measured using a pseudo free-standing tensile test). e–f) *S–S* curves from cyclic tensile tests with a fixed strain of 10% of e) D18 and f) D18$_{0.4}$:SEBS$_{0.6}$ blend films. g) Plastic strains during the repeated cycles.

= 126 vs 8%), while its PCE was 4 times greater than that of D18$_{0.2}$:SEBS$_{0.8}$/L8-BO (PCE = 12.13 vs 3.15%). In addition, it is worth noting that the D18$_{0.4}$:SEBS$_{0.6}$/L8-BO-based active layers demonstrated much greater stretchability than the previously reported high-performance OSCs with PCEs > 10%, as shown in Figure 3d.

To elucidate the important role of the D18$_x$:SEBS$_{1.0-x}$ composition on the mechanical properties, we also performed the tensile tests on the D18$_x$:SEBS$_{1.0-x}$ blend films without the L8-BO upper layer (Figure S8 and Table S5, Supporting Information). The stretchability and toughness trends of D18$_x$:SEBS$_{1.0-x}$ blend films in terms of the D18:SEBS ratio were matched well with those of the D18$_x$:SEBS$_{1.0-x}$:L8-BO PHJ films, showing significant jumps in both values around the SEBS composition of 60 wt%; D18 (COS = 23% and toughness = 6.5 MJ m^{-3}) < D18$_{0.8}$:SEBS$_{0.2}$ (COS = 32% and toughness = 6.6 MJ m^{-3}) < D18$_{0.6}$:SEBS$_{0.4}$ (COS = 41% and toughness = 7.0 MJ m^{-3}) < D18$_{0.4}$:SEBS$_{0.6}$ (COS = 247% and toughness = 15.0 MJ m^{-3}) < D18$_{0.2}$:SEBS$_{0.8}$ (COS > 600% and toughness > 25 MJ m^{-3}). This indicates that the mechanical properties of D18$_x$:SEBS$_{1.0-x}$ were well retained in D18$_x$:SEBS$_{1.0-x}$/L8-BO PHJ structures.

Another significant benefit of incorporating elastomers into active layers is that it may boost elasticity of the active layers. To assess the elasticity of the active layers during repetitive stretching cycles, we conducted cyclic tensile tests on the pristine D18 and D18$_{0.4}$:SEBS$_{0.6}$ blend film with a fixed strain of 10% (Figure 3e–g). Based on the measured *S–S* curves from the cyclic tensile tests, we estimated plastic strain values of the films at each loading/unloading cycle, which are indicatives of the degree of plastic deformation. We observed that the D18 film was entirely fractured after 3-cycles of stretching/releasing, and the plastic strain values during the first and second cycles were 7.3% and 7.0%, respectively. This indicates

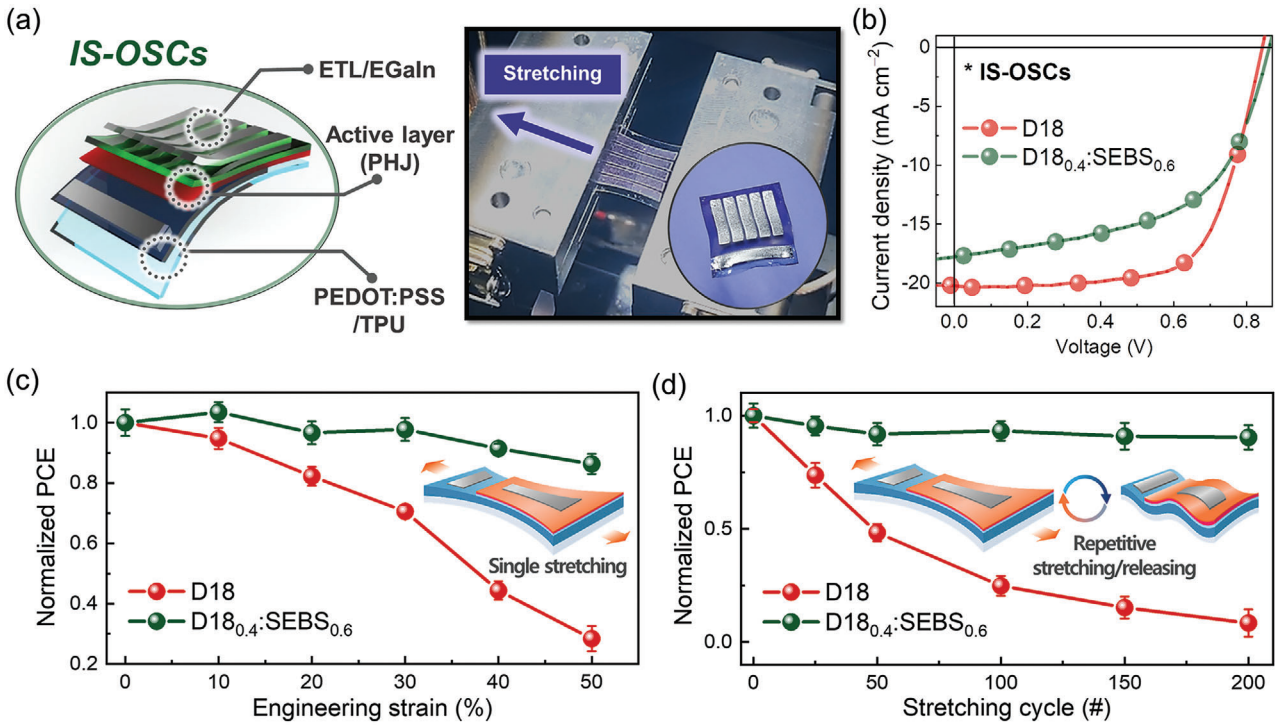

Figure 4. a) Schematic illustration and actual image of an IS-OSC device during the stretching test, b) *J–V* curves of IS-OSCs, c,d) normalized PCEs as a function of the strain c) in single stretching test, and d) in cyclic stretching test.

that the D18 films have very small elasticity (less than 3% strain). In contrast, D18$_{0.4}$:SEBS$_{0.6}$ blend film was not fractured even after 10-cycles of stretching/releasing. Although the D18$_{0.4}$:SEBS$_{0.6}$ films showed considerable plastic strains in the first and second cycles (7.4% and 4.0%, respectively), it rapidly decreased to the negative value from the third to tenth cycles, showing excellent elasticity of the films (Figure 3g). The plastic strains in the first and second cycles are presumably due to plastic deformation of D18 polymers in the blend films, and it appears that after some degree of plastic deformation of D18 polymers, the SEBS elastomers prevent further deformation of the D18 polymers in the D18$_{0.4}$:SEBS$_{0.6}$ blend film. As a consequence, the D18$_{0.4}$:SEBS$_{0.6}$-based active layer showed excellent elasticity in addition to the high photovoltaic performance, highlighting its great potentials in wearable applications necessitating resilience to repetitive body motions.

2.4. Intrinsically-Stretchable Organic Solar Cells (IS-OSCs)

To demonstrate the feasibility of the developed blend systems in wearable applications, IS-OSC devices consisting of a thermoplastic urethane (TPU) elastomer substrate with organic electrodes (poly(3,4-ethylenedioxythiophene):poly(styrenesulfonate), PEDOT:PSS) and liquid-metal electrodes (eutectic gallium indium, EGaIn) were fabricated (**Figure 4**).[3h,22] The schematic and photograph of the IS-OSC device and the measurement setups for the stretching test of the IS-OSCs are shown in Figure 4a. The photovoltaic and mechanical properties of the IS-OSCs fabricated from the reference D18/L8-BO film and the D18$_{0.4}$:SEBS$_{0.6}$/L8-BO film were investigated.

The *J–V* profiles of the IS-OSCs are shown in Figure 4b, and the photovoltaic parameters are summarized in **Table 3**. The initial PCEs of the IS-OSC devices showed the similar trend as that observed for the rigid OSC devices. The PCE of the IS-OSC based on the reference D18/L8-BO PHJ film was 11.62%, which was higher than that of the D18$_{0.4}$:SEBS$_{0.6}$/L8-BO (PCE = 8.51%). However, the discrepancy in the stretchability between two IS-OSCs was remarkable. We performed two different stretching experiments of 1) single-stretching and 2) cyclic stretching tests. In the single-stretching test, we monitored the PCE changes of two IS-OSCs as a function of the applied strain (Figure 4c). Whereas the PCE of the D18-based IS-OSCs declined rapidly when the strain increased above 10%, the D18$_{0.4}$:SEBS$_{0.6}$/L8-BO-based IS-OSCs maintained the PCE stable even at 50% strain. After 50% strain, the normalized PCEs of the former and latter devices were 0.28 and 0.86, respectively, compared to the unstrained device. Thus, at 50% strain, the PCE value of the D18$_{0.4}$:SEBS$_{0.6}$/L8-BO-based IS-OSCs was 7.31%, which was significantly higher than that of the D18/L8-BO-based IS-OSCs (PCE = 3.25%). The enhanced mechanical robustness of the D18$_{0.4}$:SEBS$_{0.6}$/L8-BO-based IS-OSCs was also proven in another important stretching test under cyclic stretching/releasing conditions (Figure 4d; Figure S9, Supporting Information). The cyclic stretching test was carried out with a fixed strain of 15%. The D18/L8-BO-based IS-OSCs have poor cyclic endurance, retaining only 8% of their original PCE after 200 cycles of stretching/releasing. In contrast, the D18$_{0.4}$:SEBS$_{0.6}$/L8-BO-based IS-OSCs showed stable operation, retaining 90% of their original PCEs after 200 cycles.

Table 3. Photovoltaic parameters and mechanical properties of IS-OSCs.

P_D:elastomer	V_{oc} [V]	J_{sc} [mA cm^{-2}]	FF	PCE$_{max(avg)}$ [b] [%]	Normalized PCE at 50% strain[b]	Normalized PCE after 200 cycles[b),c)]
D18	0.85	20.29	0.68	11.62 (11.37)	0.28	0.08
D18$_{0.4}$:SEBS$_{0.6}$	0.86	18.93	0.55	8.51 (8.30)	0.86	0.90

[a] Calculated from EQE spectra; [b] Average values obtained from 5 independent devices; [c] Cyclic stretching at a fixed strain of 15%.

2.5. Morphological Properties

To gain a deeper insight into the underlying factors contributing to the photovoltaic and mechanical properties, morphological properties of the D18$_x$:SEBS$_{1.0-x}$ blend films and D18$_x$:SEBS$_{1.0-x}$/L8-BO PHJ films were examined using transmission electron microscopy (TEM), atomic force microscopy (AFM), grazing incidence X-ray scattering (GIXS), resonant soft X-ray scattering (RSoXS), and DSC (**Figure 5** and **Figure 6**). Internal morphologies of the D18$_x$:SEBS$_{1.0-x}$ blend films at different SEBS contents was examined by obtaining TEM images (Figure 5a). To increase the contrast between two materials, we stained D18 polymers in the blend films with iodine, which selectively stains the nitrogen atoms in the D18 polymers. As a consequence, the dark and light parts in the TEM images represent D18 and SEBS domains, respectively. First, the pristine

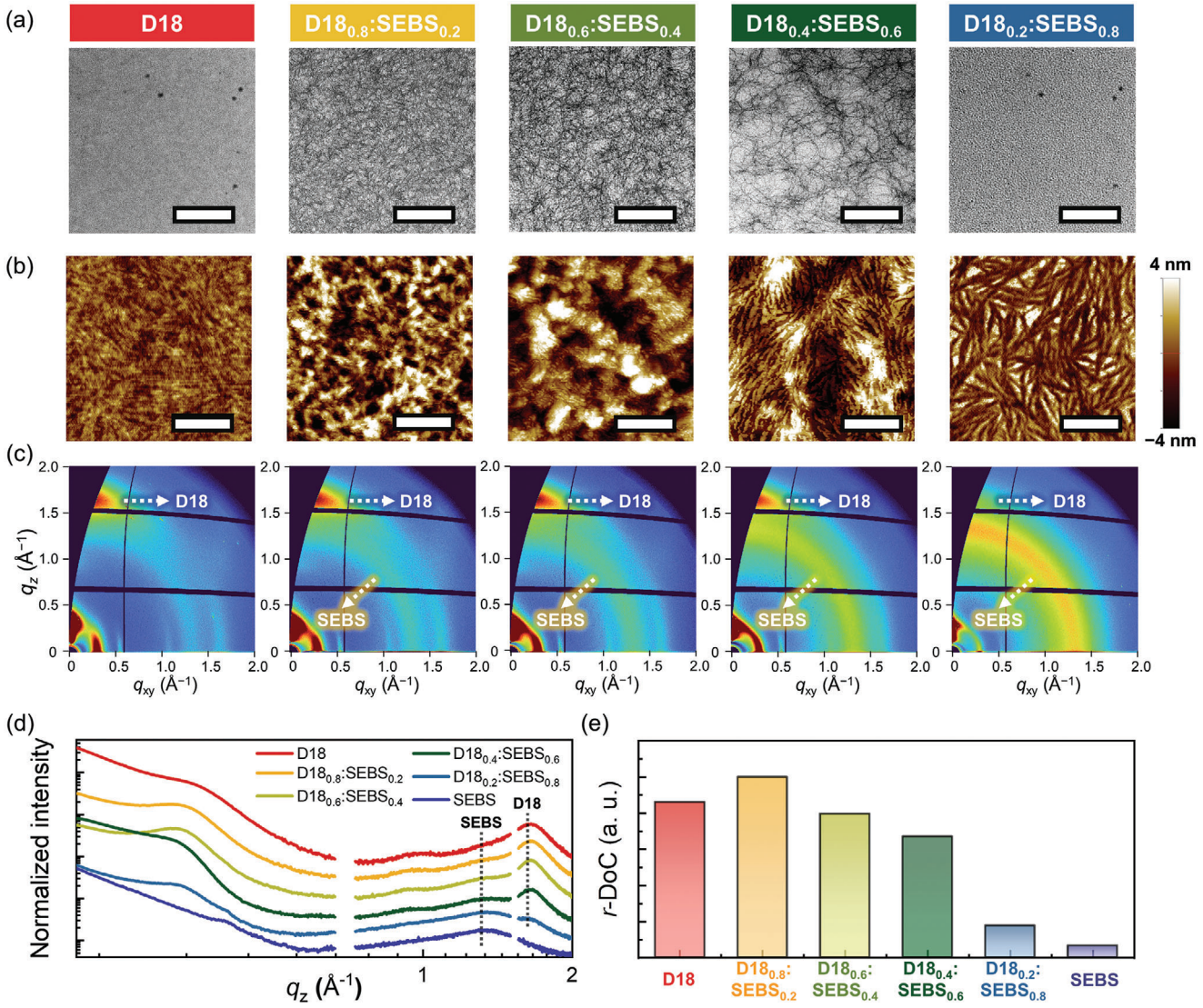

Figure 5. a) TEM images (scale bar = 100 nm), b) AFM height images (scale bar = 1 µm), c,d) GIXS c) 2D-images and d) line-cut profiles in the OOP direction of D18:SEBS blend films; e) *r*-DoC of (010) scattering peaks estimated from the GIXS profiles of D18:SEBS blend films.

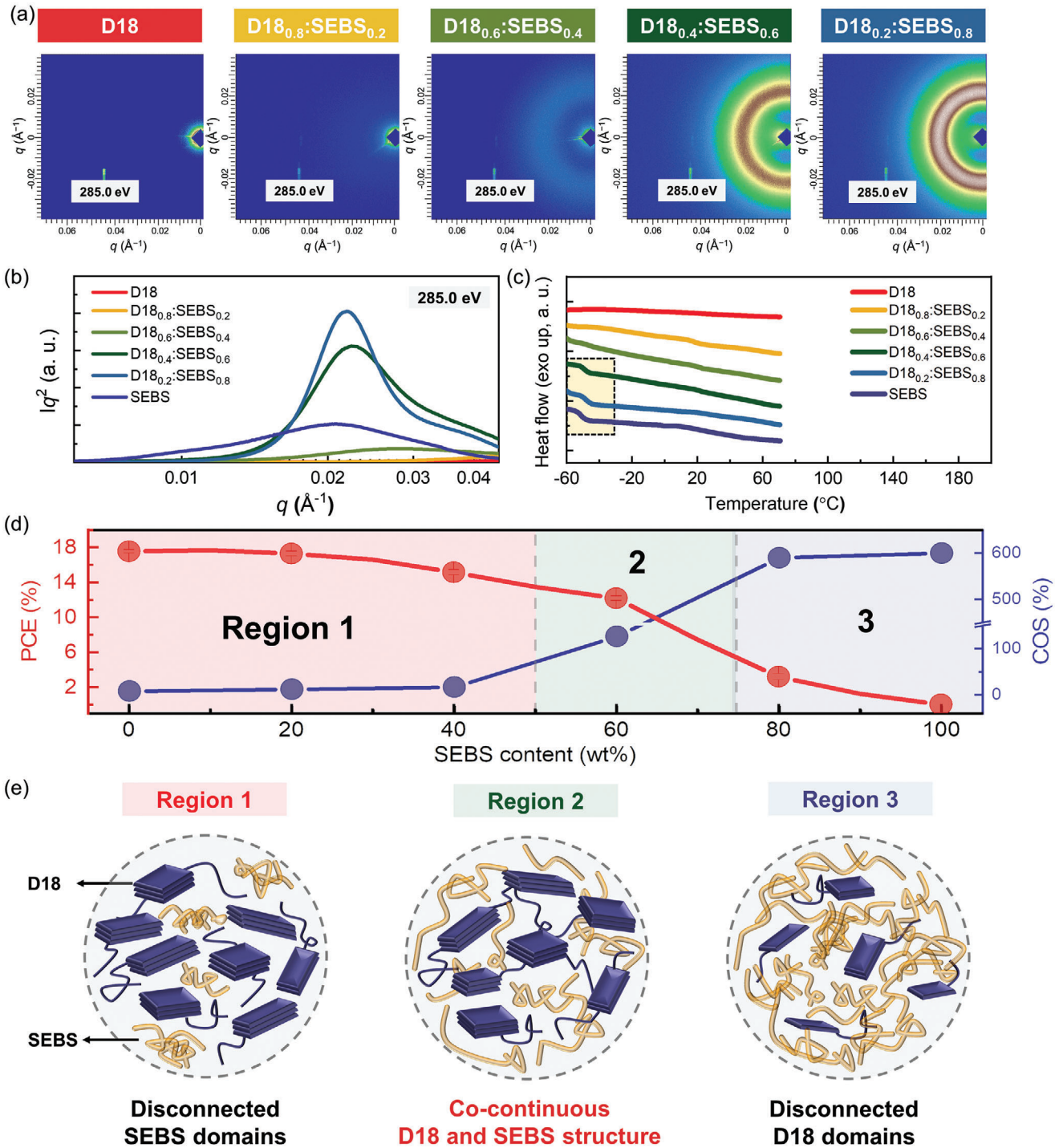

Figure 6. a,b) RSoXS a) 2D-images and b) circular averaged line-cut profiles, c) DSC 1st heating profiles of D18$_x$:SEBS$_{1.0-x}$ blend films. d) PCE versus COS plots of D18$_x$:SEBS$_{1.0-x}$/L8-BO PHJ films. e) Schematics for blend morphologies of D18$_x$:SEBS$_{1.0-x}$ blend films at different SEBS contents.

D18 did not reveal any morphology due to the absence of SEBS. In contrast, the D18$_{0.8}$:SEBS$_{0.2}$, D18$_{0.6}$:SEBS$_{0.4}$, D18$_{0.4}$:SEBS$_{0.6}$, and D18$_{0.2}$:SEBS$_{0.8}$ blend films had unique morphologies with contrasts between D18 and SEBS. While the D18$_{0.8}$:SEBS$_{0.2}$, D18$_{0.6}$:SEBS$_{0.4}$, and D18$_{0.4}$:SEBS$_{0.6}$ blend films had interconnected D18 fibril networks, the areal density of D18 fibrils became significantly reduced with increasing the SEBS content. Finally, the D18$_{0.2}$:SEBS$_{0.8}$ blend film had only scattered D18 domains in the SEBS matrix with no obvious coherence. This finding indicates that when the SEBS content exceeded 60 wt%, the D18 domains in the D18$_x$:SEBS$_{1.0-x}$ blend films became disconnected and lost their percolation. AFM height images

further corroborated these findings, showing a progressive dilution of D18 fibrils with an increase in SEBS concentration, in the order of D18, $D18_{0.8}$:$SEBS_{0.2}$, and $D18_{0.6}$:$SEBS_{0.4}$ (Figure 5b). However, with greater SEBS concentrations (i.e., $D18_{0.4}$:$SEBS_{0.6}$ and $D18_{0.2}$:$SEBS_{0.8}$), the clear fibrillar structures reappeared in the AFM height images. This is attributed to percolation and network formation of SEBS in the blend films at and beyond 60 wt% SEBS content. AFM phase images of $D18_x$:$SEBS_{1.0-x}$ blend films exhibited the same trend with the AFM height images (Figure S10, Supporting Information).

GIXS was utilized to investigate the crystalline structures of the $D18_x$:$SEBS_{1.0-x}$ and $D18_x$:$SEBS_{1.0-x}$/L8-BO thin films (Figure 5c–e). The (100) and (010) scattering peaks in the in-plane (IP) and out-of-plane (OOP) directions, respectively, indicated that pristine D18 and L8-BO exhibited a face-on preferential packing orientation (Figure 5c,d; Figures S11 and S12, Supporting Information).[23] This characteristic is advantageous for producing effective vertical charge transport. On the other hand, pristine SEBS film showed a ring-shaped, broad and isotropic scattering peak at $q = \approx 1.4$ Å^{-1}, indicating the SEBS film had amorphous packing structures (Figure S13, Supporting Information).

To examine relative crystallinity of D18 in different $D18_x$:$SEBS_{1.0-x}$ blend films, we estimated relative degree of crystallinity of D18 (010) scattering peaks (r-DoC $_{D18(010)}$, q range from 1.5 to 1.8 Å^{-1}) (Figure 5d,e; Figure S14, Supporting Information).[24] The r-DoC $_{D18(010)}$ increased from 0.86 for the D18 film to 1.00 for the $D18_{0.8}$:$SEBS_{0.2}$ film. Then, it decreased to 0.67 for the $D18_{0.4}$:$SEBS_{0.6}$ film. Interestingly, we note that when the r-DoC $_{D18(010)}$ normalized by a D18 molar fraction (r-DoC $_{D18(010)}/N_{D18}$) in each $D18_x$:$SEBS_{1.0-x}$ sample was compared, the r-DoC $_{D18(010)}/N_{D18}$ values in the $D18_{0.8}$:$SEBS_{0.2}$, $D18_{0.6}$:$SEBS_{0.4}$ and $D18_{0.4}$:$SEBS_{0.6}$ were in a range of 1.08–1.19, respectively, which were higher than that of the pristine D18 (0.86) (Table S6, Supporting Information). This indicates that the crystalline properties of D18 in the $D18_x$:$SEBS_{1.0-x}$ films were well-maintained even with the addition of 60 wt% SEBS content, which were attributed to the combined contributions from 1) strongly-preserved D18 crystalline networks and 2) the confinement effects by the SEBS domains in the $D18_x$:$SEBS_{1.0-x}$ films. In contrast, when the SEBS content exceeds 60 wt%, the relative crystallinity of D18 in $D18_x$:$SEBS_{1.0-x}$ blend films rapidly dropped, showing r-DoC $_{D18(010)} = 0.17$ and r-DoC $_{D18(010)}/N_{D18} = 0.52$, respectively, for the $D18_{0.2}$:$SEBS_{0.8}$ film. This observation agrees well with the trend in TEM images. The crystalline structures in the $D18_x$:$SEBS_{1.0-x}$/L8-BO PHJ films as a function of D18:SEBS ratio followed the same trend to that observed in the $D18_x$:$SEBS_{1.0-x}$ blend films without L8-BO. For example, the π-π scattering peaks of D18 in the $D18_x$:$SEBS_{1.0-x}$/L8-BO were distinct until 60 wt% of the SEBS content. However, the peaks became significantly diminished for the $D18_{0.2}$:$SEBS_{0.8}$/L8-BO film (Figures S15 and S16, Supporting Information).

To better understand the phase behavior of SEBS polymers in the $D18_x$:$SEBS_{1.0-x}$ blend films depending on the D18:SEBS ratio, we monitored the variation in the SEBS amorphous peaks. While the intensity of the amorphous peaks gradually increased with increasing the SEBS content, the peaks became prominent in the blend film once the SEBS content at and beyond 60 wt%. For example, the ratio ($A_{SEBS}/A_{D18(010)}$) of the area of the SEBS amorphous scattering peak at $q \approx 1.4$ Å^{-1} to that of the D18 (010) scattering peak at $q \approx 1.7$ Å^{-1} increased by 2.5-fold from $A_{SEBS}/A_{D18(010)} = 0.4$ for the $D18_{0.6}$:$SEBS_{0.4}$ to 1.0 for the $D18_{0.4}$:$SEBS_{0.6}$ film (Figure S17 and Table S6, Supporting Information). This indicates the significant development of the SEBS fibrils in the $D18_{0.6}$:$SEBS_{0.4}$ film, which aligns with the observation in AFM images showing the appearance of distinct SEBS fibrillar structures at and beyond 60 wt% SEBS content (Figure 5b; Figure S10, Supporting Information).

RSoXS measurements were also utilized to better understand the phase behaviors of D18 and SEBS in the $D18_x$:$SEBS_{1.0-x}$ blend films in terms of the domain size and purity. The RSoXS profiles were obtained at a beam energy of 285.0 eV, which maximizes material contrast between D18 and SEBS.[6c,25] The RSoXS 2D-images and circular-averaged line-cut profiles of the $D18_x$:$SEBS_{1.0-x}$ films are shown in Figure 6a,b, respectively. Pristine D18 film exhibited no discernible scattering peaks in the RSoXS profiles. On the other hand, the pristine SEBS film showed a distinct scattering peak at $q = \approx 0.02$ Å^{-1}, which corresponds to a characteristic domain size of ≈15 nm.[6c,26] This scattering peak is attributed to the material contrast that exists between the poly(styrene) and poly(ethylene-*ran*-butylene) blocks in the SEBS block copolymers. While $D18_{0.8}$:$SEBS_{0.2}$ and $D18_{0.6}$:$SEBS_{0.4}$ films did not show discernible peaks, the scattering peak at $q = \approx 0.02$ Å^{-1} became distinct for the $D18_{0.4}$:$SEBS_{0.6}$ and $D18_{0.2}$:$SEBS_{0.8}$ blend films with higher SEBS content. In support of the observations from the AFM and GIXS measurements, this RSoXS result suggests that a distinct SEBS network structure appear once the SEBS content exceeds 60 wt% as shown in both Figure 6a,b. The RSoXS profiles of $D18_x$:$SEBS_{1.0-x}$/L8-BO PHJ films as a function of D18:SEBS ratio followed the same trend to that in the $D18_x$:$SEBS_{1.0-x}$ blend films (Figure S18, Supporting Information). This result suggests that the domain properties and phase structures of $D18_x$:$SEBS_{1.0-x}$ at different composition ratios are well maintained after the deposition of L8-BO top layers.

Crystalline behaviors of SEBS in the $D18_x$:$SEBS_{1.0-x}$ blend films were examined using DSC measurements (Figure 6c). As stated in the preceding section, the SEBS exhibited a T_g of ≈−55 °C that originated from poly(ethylene-*ran*-butylene) blocks. However, D18 did not show any distinct peak during the DSC 2nd heating cycle. In order to correlate the crystalline properties of the $D18_x$:$SEBS_{1.0-x}$ blend films with the OSC performance, all the samples were produced under the same condition as the OSC fabrication and then, the samples were collected in each DSC pan for the measurements. The first heating cycles of the blend films were investigated to obtain the crystalline behaviors of the as-cast films with residual thermal history. In the DSC profiles, the $D18_{0.8}$:$SEBS_{0.2}$ and $D18_{0.6}$:$SEBS_{0.4}$ blends did not show the peak associated with the T_g of SEBS. In contrast, the $D18_{0.4}$:$SEBS_{0.6}$ and $D18_{0.2}$:$SEBS_{0.8}$ blends exhibited distinct T_g peaks of SEBS. This suggests that distinct SEBS structures were formed in the $D18_x$:$SEBS_{1.0-x}$ films when the SEBS content was 60 wt% or higher.

Next, the contact angles of water and glycerol droplets on the surfaces of D18, L8-BO, and SEBS films were measured (Figure S19, Supporting Information). By utilizing these contact-angle values, the interfacial tension (γ) between the active components (D18 and L8-BO) and SEBS was calculated to assess their

molecular compatibility (Table S7, Supporting Information). The γ value between D18 and SEBS (1.95 mN m^{-1}) is lower than that between L8-BO and SEBS (3.25 mN m^{-1}), indicating that D18 exhibits greater molecular compatibility with SEBS than that between the L8-BO and SEBS. This supports the use of a PHJ-type active layer structure in this study, which excludes L8-BO in the $D18_x$:$SEBS_{1.0-x}$ bottom layer, facilitates the efficient percolation between D18 and SEBS at their optimal composition ratio (i.e., 40:60, w/w).

Figure 6d presents a summary of the trends observed in photovoltaic and mechanical performance for the $D18_x$:$SEBS_{1.0-x}$ blend films as a function of SEBS content. From these trends, the D18:SEBS films are classified into three distinct regions, each correlating with morphological changes in the D18:SEBS structures. as illustrated in Figure 6e. In region 1 (SEBS contents ranging from 0 to 40 wt%), the $D18_x$:$SEBS_{1.0-x}$/L8-BO-based OSCs exhibit high PCEs of > 15%, but show limited stretchability (COS < 20%) (Figure 6d). The limited stretchability, despite the presence of SEBS, is due to lack of interconnected SEBS networks necessary for efficient mechanical stress dissipation (Figure 6e). On the contrary, in region 3 (SEBS contents > 80 wt%), the $D18_x$:$SEBS_{1.0-x}$/L8-BO-based OSCs demonstrate remarkable mechanical stretchability (COS > 600%), but significantly lower PCE values (< 3%). The poor PCE in this region is due to the sparse and disconnected D18 domains within the SEBS matrix, leading to inadequate charge transport channels. Meanwhile, the OSCs in region 2 achieve a balance, affording a significant PCE (12.13%) and stretchability (COS = 126%) at the same time. The optimal composition ratio of D18 and SEBS in blend films facilitates the formation of co-continuous domains, allowing for effective construction of both electrical (through crystalline fibril networks of D18) and mechanical scaffold (through well-connected SEBS networks). This leads to the formation of active layers that provide efficient charge transport and mechanical stress dissipation suitable for the high-performance IS-OSCs with extreme stretchability.

3. Conclusions

In conclusion, we successfully developed high-performance IS-OSCs characterized by exceptional mechanical stretchability and cyclic durability. These results were achieved by constructing co-continuous networks of D18 and SEBS within the PHJ-type $D18_x$:$SEBS_{1.0-x}$/L8-BO active layers. Through comprehensive morphological characterizations, we have demonstrated that the co-continuous morphology can be achieved at a specific composition ratio between the two polymers (D18:SEBS = 40:60 w/w), resulting in well-connected mechanical and electrical channels. Consequently, the $D18_{0.4}$:$SEBS_{0.6}$/L8-BO-based OSCs exhibited 16-time greater stretchability (COS = 126%) compared to the D18/L8-BO-based OSCs (COS = 8%), and a 4-time higher PCE (12.13%) than the OSCs based on the SEBS-rich active layers ($D18_{0.2}$:$SEBS_{0.8}$/L8-BO, PCE = 3.15%). Furthermore, the $D18_{0.4}$:$SEBS_{0.6}$/L8-BO-based IS-OSCs exhibited outstanding device stretchability in wearable applications, showing 86% retention of the initial PCE at 50% strain and 90% retention of the initial PCE after 200-times stretching/releasing cycles with 15% strain, which positioned them among one of the best IS-OSCs in terms of the stretchability.

Supporting Information

Supporting Information is available from the Wiley Online Library or from the author.

Acknowledgements

J.-W.L. and Q.N. contributed equally to this work. This work was supported by the National Research Foundation of Korea (NRF-2020M3H4A1A02084906 and RS-2023-00217884). This research used resources of the Advanced Light Source, which is a DOE Office of Science User Facility under contract no. DE-AC02-05CH11231.

Conflict of Interest

The authors declare no conflict of interest.

Data Availability Statement

The data that support the findings of this study are available from the corresponding author upon reasonable request.

Keywords

elastomer, intrinsically stretchable organic solar cells, mechanical robustness, polymer solar cells, stretchability

Received: March 15, 2024
Revised: April 16, 2024
Published online: May 13, 2024

[1] a) B. Kippelen, J.-L. Brédas, *Energy Environ. Sci.* **2009**, *2*, 251; b) O. Inganäs, *Adv. Mater.* **2018**, *30*, 1800388; c) C. Sun, J.-W. Lee, C. Lee, D. Lee, S. Cho, S.-K. Kwon, B. J. Kim, Y.-H. Kim, *Joule* **2023**, *7*, 416; d) Y. Li, G. Xu, C. Cui, Y. Li, *Adv. Energy Mater.* **2018**, *8*, 1701791; e) D. J. Lipomi, *Joule* **2018**, *2*, 195; f) S. Yoon, S. Park, S. H. Park, S. Nah, S. Lee, J.-W. Lee, H. Ahn, H. Yu, E.-Y. Shin, B. J. Kim, B. K. Min, J. H. Noh, H. J. Son, *Joule* **2022**, *6*, 2406; g) E. Dauzon, X. Sallenave, C. Plesse, F. Goubard, A. Amassian, T. D. Anthopoulos, *Adv. Mater.* **2021**, *33*, 2101469; h) S. Dong, T. Jia, K. Zhang, J. Jing, F. Huang, *Joule* **2004**, *4*, 2020. i) X. Zheng, L. Zuo, F. Zhao, Y. Li, T. Chen, S. Shan, K. Yan, Y. Pan, B. Xu, C.-Z. Li, M. Shi, J. Hou, H. Chen, *Adv. Mater.* **2022**, *34*, 2200044.

[2] a) Q. Liu, Y. Jiang, K. Jin, J. Qin, J. Xu, W. Li, J. Xiong, J. Liu, Z. Xiao, K. Sun, S. Yang, X. Zhang, L. Ding, *Sci. Bull.* **2020**, *65*, 272; b) Y. Cui, Y. Xu, H. Yao, P. Bi, L. Hong, J. Zhang, Y. Zu, T. Zhang, J. Qin, J. Ren, Z. Chen, C. He, X. Hao, Z. Wei, J. Hou, *Adv. Mater.* **2021**, *33*, 2102420; c) J.-W. Lee, C. Sun, T. N.-L. Phan, D. C. Lee, Z. Tan, H. Jeon, S. Cho, S.-K. Kwon, Y.-H. Kim, B. J. Kim, *Energy Environ. Sci.* **2023**, *16*, 3339; d) C. Li, J. Zhou, J. Song, J. Xu, H. Zhang, X. Zhang, J. Guo, L. Zhu, D. Wei, G. Han, J. Min, Y. Zhang, Z. Xie, Y. Yi, H. Yan, F. Gao, F. Liu, Y. Sun, *Nat. Energy* **2021**, *6*, 605; e) F. Liu, L. Zhou, W. Liu, Z. Zhou, Q. Yue, W. Zheng, R. Sun, W. Liu, S. Xu, H. Fan, L. Feng, Y. Yi, W. Zhang, X. Zhu, *Adv. Mater.* **2021**, *33*, 2100830; f) Y. Cui, H. Yao, J. Zhang, K. Xian, T. Zhang, L. Hong, Y. Wang, Y. Xu, K. Ma, C. An, C. He, Z. Wei, F. Gao, J. Hou, *Adv. Mater.* **2020**, *32*, 1908205; g) L. Zhan, S. Li, X. Xia, Y. Li, X. Lu, L. Zuo, M. Shi, H. Chen, *Adv. Mater.* **2021**, *33*, 2007231; h) L. Zhu, M. Zhang, J. Xu, C. Li, J. Yan, G. Zhou, W. Zhong, T. Hao, J. Song, X. Xue, Z. Zhou, R. Zeng, H. Zhu, C.-C. Chen, R. C. I. MacKenzie, Y.

Zou, J. Nelson, Y. Zhang, Y. Sun, F. Liu, *Nat. Mater.* **2022**, *21*, 656; i) H. Lu, W. Liu, G. Ran, Z. Liang, H. Li, N. Wei, H. Wu, Z. Ma, Y. Liu, W. Zhang, X. Xu, Z. Bo, *Angew. Chem., Int. Ed.* **2024**, 202314420; j) S. Luo, C. Li, J. Zhang, X. Zou, H. Zhao, K. Ding, H. Huang, J. Song, J. Yi, H. Yu, K. S. Wong, G. Zhang, H. Ade, W. Ma, H. Hu, Y. Sun, H. Yan, *Nat. Commun.* **2023**, *14*, 6964; k) C. Sun, J.-W. Lee, Z. Tan, T. N.-L. Phan, D. Han, H.-G. Lee, S. Lee, S.-K. Kwon, B. J. Kim, Y.-H. Kim, *Adv. Energy Mater.* **2023**, *13*, 2301283; l) S. Bao, H. Yang, H. Fan, J. Zhang, Z. Wei, C. Cui, Y. Li, *Adv. Mater.* **2021**, *33*, 2105301; m) Z. Gan, L. Wang, J. Cai, C. Guo, C. Chen, D. Li, Y. Fu, B. Zhou, Y. Sun, C. Liu, J. Zhou, D. Liu, W. Li, T. Wang, *Nat. Commun.* **2023**, *14*, 6297; n) J.-W. Lee, C. Sun, J. Lee, D. J. Kim, W. J. Kang, S. Lee, D. Kim, J. Park, T. N.-L. Phan, Z. Tan, F. S. Kim, J.-Y. Lee, X. Bao, T.-S. Kim, Y.-H. Kim, B. J. Kim, *Adv. Energy Mater.* **2024**, *14*, 2303872; o) B. Liu, W. Xu, R. Ma, J.-W. Lee, T. A. Dela Peña, W. Yang, B. Li, M. Li, J. Wu, Y. Wang, C. Zhang, J. Yang, J. Wang, S. Ning, Z. Wang, J. Li, H. Wang, G. Li, B. J. Kim, L. Niu, X. Guo, H. Sun, *Adv. Mater.* **2023**, *35*, 2308334; p) S. H. Chen, S. T. Zhu, L. Hong, W. Y. Deng, Y. Zhang, Y. Fu, Z. Y. Zhong, M. H. Dong, C. C. Liu, X. H. Lu, K. Zhang, F. Huang, *Angew. Chem., Int. Ed.* **2024**, 202318756.

[3] a) Y. T. Hsieh, J. Y. Chen, S. Fukuta, P. C. Lin, T. Higashihara, C. C. Chueh, W. C. Chen, *ACS Appl. Mater. Interfaces* **2018**, *10*, 21712; b) Z. Jiang, K. Fukuda, W. C. Huang, S. Park, R. Nur, M. O. G. Nayeem, K. Yu, D. Inoue, M. Saito, H. Kimura, T. Yokota, S. Umezu, D. Hashizume, I. Osaka, K. Takimiya, T. Someya, *Adv. Funct. Mater.* **2019**, *29*, 1808378; c) J.-W. Lee, G. U. Kim, D. J. Kim, Y. Jeon, S. Li, T. S. Kim, J. Y. Lee, B. J. Kim, *Adv. Energy Mater.* **2022**, *12*, 2200887; d) J. M. Huang, Z. Lu, J. Q. He, H. Hu, Q. Liang, K. Liu, Z. W. Ren, Y. K. Zhang, H. Y. Yu, Z. J. Zheng, G. Li, *Energy Environ. Sci.* **2023**, *16*, 1251; e) Z. Y. Wang, M. C. Xu, Z. L. Li, Y. R. Gao, L. Yang, D. Zhang, M. Shao, *Adv. Funct. Mater.* **2021**, *31*, 2103534; f) S. Seo, J.-W. Lee, D. J. Kim, D. Lee, T. N. L. Phan, J. Park, Z. P. Tan, S. Cho, T. S. Kim, B. J. Kim, *Adv. Mater.* **2023**, *35*, 2300230; g) J.-W. Lee, S. Seo, S.-W. Lee, G.-U. Kim, S. Han, T. N.-L. Phan, S. Lee, S. Li, T.-S. Kim, J.-Y. Lee, B. J. Kim, *Adv. Mater.* **2022**, *34*, 2207544; h) Z. Wang, M. Xu, Z. Li, Y. Gao, L. Yang, D. Zhang, M. Shao, *Adv. Funct. Mater.* **2021**, *31*, 2103534.

[4] a) J. Wang, Y. Cui, Y. Xu, K. Xian, P. Bi, Z. Chen, K. Zhou, L. Ma, T. Zhang, Y. Yang, Y. Zu, H. Yao, X. Hao, L. Ye, J. Hou, *Adv. Mater.* **2022**, *34*, 2205009; b) J.-W. Lee, C. Sun, B. S. Ma, H. J. Kim, C. Wang, J. M. Ryu, C. Lim, T.-S. Kim, Y.-H. Kim, S.-K. Kwon, B. J. Kim, *Adv. Energy Mater.* **2021**, *11*, 2003367; c) H. You, A. L. Jones, B. S. Ma, G.-U. Kim, S. Lee, J.-W. Lee, H. Kang, T.-S. Kim, J. R. Reynolds, B. J. Kim, *J. Mater. Chem. A* **2021**, *9*, 2775; d) R. Ma, K. Zhou, Y. Sun, T. Liu, Y. Kan, Y. Xiao, T. A. Dela Peña, Y. Li, X. Zou, Z. Xing, Z. Luo, K. S. Wong, X. Lu, L. Ye, H. Yan, K. Gao, *Matter* **2022**, *5*, 725; e) W. Song, K. Yu, J. Ge, L. Xie, R. Zhou, R. Peng, X. Zhang, M. Yang, Z. Wei, Z. Ge, *Matter* **2022**, *5*, 1877; f) S. Siddika, Z. Peng, N. Balar, X. Dong, X. Zhong, W. You, H. Ade, B. T. O'Connor, *Joule* **2023**, *7*, 1593.

[5] a) Z. Peng, K. Xian, Y. Cui, Q. Qi, J. Liu, Y. Xu, Y. Chai, C. Yang, J. Hou, Y. Geng, L. Ye, *Adv. Mater.* **2021**, *33*, 2106732; b) J. Wang, C. Han, F. Bi, D. Huang, Y. Wu, Y. Li, S. Wen, L. Han, C. Yang, X. Bao, J. Chu, *Energy Environ. Sci.* **2021**, *14*, 5968; c) L. Ma, Y. Cui, J. Zhang, K. Xian, Z. Chen, K. Zhou, T. Zhang, W. Wang, H. Yao, S. Zhang, X. Hao, L. Ye, J. Hou, *Adv. Mater.* **2023**, *35*, 2208926; d) J.-W. Lee, C. Sun, D. J. Kim, M. Y. Ha, D. Han, J. S. Park, C. Wang, W. B. Lee, S.-K. Kwon, T.-S. Kim, Y.-H. Kim, B. J. Kim, *ACS Nano* **2021**, *15*, 19970; e) J. Wang, Y. Wang, K. Xian, J. Qiao, Z. Chen, P. Bi, T. Zhang, Z. Zheng, X. Hao, L. Ye, S. Zhang, J. Hou, *Adv. Mater.* **2024**, *36*, 2305424; f) Q. Zhu, J. Xue, G. Lu, B. Lin, H. B. Naveed, Z. Bi, G. Lu, W. Ma, *Nano Energy* **2022**, *97*, 107194; g) J.-W. Lee, S.-W. Lee, J. Kim, Y. H. Ha, C. Sun, T. Ngoc-Lan Phan, S. Lee, C. Wang, T.-S. Kim, Y.-H. Kim, B. J. Kim, *J. Mater. Chem. A* **2022**, *10*, 20312; h) Q. Zhu, J. Xue, H. Zhao, B. Lin, Z. Bi, S. Seibt, K. Zhou, W. Ma, *J. Mater. Chem. A* **2022**, *10*, 8293; i) J.-W. Lee, C. Lim, S.-W. Lee, Y. Jeon, S. Lee, T.-S. Kim, J.-Y. Lee, B. J. Kim, *Adv. Energy Mater.* **2022**, *12*, 2202224; j) C. Yan, J. Qin, Y. Wang, G. Li, P. Cheng, *Adv. Energy Mater.* **2022**, *12*, 2201087.

[6] a) W. Tang, Z. Ding, Y. Su, Q. Weng, Y. Zhang, R. Li, W. Huang, Z. Wang, Y. Wu, Y. Han, K. Zhao, Z. Yang, X. Wang, S. Liu, *Adv. Funct. Mater.* **2024**, 2312289; b) S. Li, M. Gao, K. Zhou, X. Li, K. Xian, W. Zhao, Y. Chen, C. He, L. Ye, *Adv. Mater.* **2024**, *36*, 2307278; c) A. A. Shafe, H. M. Schrickx, K. Ding, H. Ade, B. T. O'Connor, *ACS Energy Lett.* **2023**, *8*, 3720; d) S. Seo, J.-W. Lee, D. J. Kim, D. Lee, T. N.-L. Phan, J. Park, Z. Tan, S. Cho, T.-S. Kim, B. J. Kim, *Adv. Mater.* **2023**, *35*, 2300230; e) C. Liu, C. Xiao, C. Xie, Q. Zhu, Q. Chen, W. Ma, W. Li, *ChemPhysChem* **2022**, *23*, 202100725; f) Z. Xu, Y. Han, Y. Bai, X. Chen, J. Guo, L. Zhang, C. Gong, Q. Luo, T. Zhang, C.-Q. Ma, *npj Flex. Electron.* **2022**, *6*, 56.

[7] a) S. Tang, Y. Xu, G. Su, J. Bao, A. Zhang, *RSC Adv.* **2018**, *8*, 35429; b) J.-W. Lee, B. S. Ma, H. J. Kim, T.-S. Kim, B. J. Kim, *JACS Au* **2021**, *1*, 612; c) N. Balar, J. J. Rech, R. Henry, L. Ye, H. Ade, W. You, B. T. O'Connor, *Chem. Mater.* **2019**, *31*, 5124.

[8] a) M. Gao, J. Wu, X. Yuan, C. He, H. Jiang, W. Zhao, C. Duan, Y. Chen, Y. Ke, H. Yao, L. Ye, *Energy Environ. Sci.* **2023**, *16*, 5822; b) J. Han, F. Bao, D. Huang, X. Wang, C. Yang, R. Yang, X. Jian, J. Wang, X. Bao, J. Chu, *Adv. Funct. Mater.* **2020**, *30*, 2003654.

[9] a) E. Dauzon, X. Sallenave, C. Plesse, F. Goubard, A. Amassian, T. D. Anthopoulos, *J. Mater. Chem. C* **2022**, *10*, 3375; b) J.-W. Lee, H.-G. Lee, E. S. Oh, S.-W. Lee, T. N.-L. Phan, S. Li, T.-S. Kim, B. J. Kim, *Joule* **2024**, *8*, 204; c) J. Wang, C. Han, J. Han, F. Bi, X. Sun, S. Wen, C. Yang, C. Yang, X. Bao, J. Chu, *Adv. Energy Mater.* **2022**, *12*, 2201614.

[10] a) S. A. Mollinger, B. A. Krajina, R. Noriega, A. Salleo, A. J. Spakowitz, *ACS Macro Lett.* **2015**, *4*, 708; b) L. Ye, S. Li, X. Liu, S. Zhang, M. Ghasemi, Y. Xiong, J. Hou, H. Ade, *Joule* **2019**, *3*, 443; c) J. Xu, S. H. Wang, G. J. N. Wang, C. X. Zhu, S. C. Luo, L. H. Jin, X. D. Gu, S. C. Chen, V. R. Feig, J. W. F. To, S. Rondeau-Gagne, J. Park, B. C. Schroeder, C. Lu, J. Y. Oh, Y. M. Wang, Y. H. Kim, H. Yan, R. Sinclair, D. S. Zhou, G. Xue, B. Murmann, C. Linder, W. Cai, J. B. H. Tok, J. W. Chung, Z. N. Bao, *Science* **2017**, *355*, 59; d) D. J. Kang, H. Kang, K.-H. Kim, B. J. Kim, *ACS Nano* **2012**, *6*, 7902; e) M. Z. Seyedin, J. M. Razal, P. C. Innis, G. G. Wallace, *Adv. Funct. Mater.* **2014**, *24*, 2957.

[11] S. Nikzad, H.-C. Wu, J. Kim, C. M. Mahoney, J. R. Matthews, W. Niu, Y. Li, H. Wang, W.-C. Chen, M. F. Toney, M. He, Z. Bao, *Chem. Mater.* **2020**, *32*, 897.

[12] a) Y. Kazemi, A. Ramezani Kakroodi, A. Ameli, T. Filleter, C. B. Park, *J. Mater. Chem. C* **2018**, *6*, 350; b) D. Choi, H. Kim, N. Persson, P.-H. Chu, M. Chang, J.-H. Kang, S. Graham, E. Reichmanis, *Chem. Mater.* **2016**, *28*, 1196; c) M. Wang, P. Baek, A. Akbarinejad, D. Barker, J. Travas-Sejdic, *J. Mater. Chem. C* **2019**, *7*, 5534.

[13] a) S. M. Liff, N. Kumar, G. H. McKinley, *Nat. Mater.* **2007**, *6*, 76; b) H. Koerner, G. Price, N. A. Pearce, M. Alexander, R. A. Vaia, *Nat. Mater.* **2004**, *3*, 115; c) S. Maiti, N. K. Shrivastava, B. B. Khatua, *Polym. Compos.* **2013**, *34*, 570.

[14] a) J. Zhang, H. Mao, K. Zhou, L. Zhang, D. Luo, P. Wang, L. Ye, Y. Chen, *Adv. Mater.* **2024**, *36*, 2309379; b) K. Jiang, J. Zhang, C. Zhong, F. R. Lin, F. Qi, Q. Li, Z. Peng, W. Kaminsky, S.-H. Jang, J. Yu, X. Deng, H. Hu, D. Shen, F. Gao, H. Ade, M. Xiao, C. Zhang, A. K. Y. Jen, *Nat. Energy* **2022**, *7*, 1076; c) J. Chen, J. Cao, L. Liu, L. Xie, H. Zhou, J. Zhang, K. Zhang, M. Xiao, F. Huang, *Adv. Funct. Mater.* **2022**, *32*, 2200629; d) W. Gao, F. Qi, Z. Peng, F. R. Lin, K. Jiang, C. Zhong, W. Kaminsky, Z. Guan, C.-S. Lee, T. J. Marks, H. Ade, A. K.-Y. Jen, *Adv. Mater.* **2022**, *34*, 2202089.

[15] a) G. Polacco, A. Muscente, D. Biondi, S. Santini, *Eur. Polym. J.* **2006**, *42*, 1113; b) H. Tran, V. R. Feig, K. Liu, Y. Zheng, Z. Bao, *Macromolecules* **2019**, *52*, 3965.

[16] J. Xu, H.-C. Wu, C. Zhu, A. Ehrlich, L. Shaw, M. Nikolka, S. Wang, F. Molina-Lopez, X. Gu, S. Luo, D. Zhou, Y.-H. Kim, G.-J. N. Wang, K. Gu, V. R. Feig, S. Chen, Y. Kim, T. Katsumata, Y.-Q. Zheng, H. Yan, J. W. Chung, J. Lopez, B. Murmann, Z. Bao, *Nat. Mater.* **2019**, *18*, 594.

[17] C. A. Sierra, C. Galán, J. G. Fatou, M. D. Parellada, J. A. Barrio, *Polymer* **1997**, *38*, 4325.
[18] J.-H. Kim, A. Nizami, Y. Hwangbo, B. Jang, H.-J. Lee, C.-S. Woo, S. Hyun, T.-S. Kim, *Nat. Commun.* **2013**, *4*, 2520.
[19] a) Z. Chiguvare, V. Dyakonov, *Phys. Rev. B* **2004**, *70*, 235207; b) H. Sun, H. Yu, Y. Shi, J. Yu, Z. Peng, X. Zhang, B. Liu, J. Wang, R. Singh, J. Lee, Y. Li, Z. Wei, Q. Liao, Z. Kan, L. Ye, H. Yan, F. Gao, X. Guo, *Adv. Mater.* **2020**, *32*, 2004183.
[20] a) J. Ko, Y. Kim, J. S. Kang, R. Berger, H. Yoon, K. Char, *Adv. Mater.* **2020**, *32*, 1908087; b) J. Ko, R. Berger, H. Lee, H. Yoon, J. Cho, K. Char, *Chem. Soc. Rev.* **2021**, *50*, 3585.
[21] J. Zhang, H. S. Tan, X. Guo, A. Facchetti, H. Yan, *Nat. Energy* **2018**, *3*, 720.
[22] a) J. Lee, J.-W. Lee, H. Song, M. Song, J. Park, G.-U. Kim, D. Jeong, T.-S. Kim, B. J. Kim, *J. Mater. Chem. A* **2023**, *11*, 12846; b) J.-W. Lee, C. Sun, S.-W. Lee, G.-U. Kim, S. Li, C. Wang, T.-S. Kim, Y.-H. Kim, B. J. Kim, *Energy Environ. Sci.* **2022**, *15*, 4672.
[23] a) W. Ma, G. Yang, K. Jiang, J. H. Carpenter, Y. Wu, X. Meng, T. McAfee, J. Zhao, C. Zhu, C. Wang, H. Ade, H. Yan, *Adv. Energy Mater.* **2015**, *5*, 1501400; b) Y. Li, M. Kim, Z. Wu, C. Lee, Y. W. Lee, J.-W. Lee, Y. J. Lee, E. Wang, B. J. Kim, H. Y. Woo, *J. Mater. Chem. C* **2019**, *7*, 1681.
[24] a) L. Zeng, M. Zhang, M. Gao, L. Xue, H. Wang, Z.-G. Zhang, L. Ye, *J. Mater. Chem. A* **2023**, *11*, 24184; b) F. Sun, X. Zheng, T. Hu, J. Wu, M. Wan, Y. Xiao, T. Cong, Y. Li, B. Xiao, J. Shan, E. Wang, X. Wang, R. Yang, *Energy Environ. Sci.* **2024**, *17*, 1916.
[25] B. Fan, X. Du, F. Liu, W. Zhong, L. Ying, R. Xie, X. Tang, K. An, J. Xin, N. Li, W. Ma, C. J. Brabec, F. Huang, Y. Cao, *Nat. Energy* **2018**, *3*, 1051.
[26] C. He, Y. Pan, G. Lu, B. Wu, X. Xia, C.-Q. Ma, Z. Chen, H. Zhu, X. Lu, W. Ma, L. Zuo, H. Chen, *Adv. Mater.* **2022**, *34*, 2203379.